Pressure-induced amorphization and existence of molecular and polymeric amorphous forms in dense SO_2

Huichao Zhang[a,b], Ondrej Tóth[c], Xiao-Di Liu[a,1], Roberto Bini[d,e], Eugene Gregoryanz[a,f,g,h], Philip Dalladay-Simpson[h], Simone De Panfilis[i], Mario Santoro[a,e,j,1], Federico Aiace Gorelli[a,e,j,1], and Roman Martoňák[c,1]

[a]Key Laboratory of Materials Physics, Institute of Solid State Physics, Chinese Academy of Sciences, Hefei 230031, China; [b]University of Science and Technology of China, Hefei 230026, China; [c]Department of Experimental Physics, Faculty of Mathematics, Physics and Informatics, Comenius University, 842 48 Bratislava, Slovakia; [d]Department of Chemistry, University of Florence, 50121 Florence, Italy; [e]European Laboratory for Non-Linear Spectroscopy, 50019 Sesto Fiorentino, Italy; [f]School of Physics and Astronomy, University of Edinburgh, Edinburgh EH9 3JZ, United Kingdom; [g]Centre for Science at Extreme Conditions, University of Edinburgh, Edinburgh EH9 3JZ, United Kingdom; [h]Center for High Pressure Science Technology Advanced Research, Shanghai, 201203, China; [i]Centre for Life Nano Science, Istituto Italiano di Tecnologia, 00161 Rome, Italy; and [j]Istituto Nazionale di Ottica, Consiglio Nazionale delle Ricerche (CNR-INO), 50125 Florence, Italy

Edited by Michael L. Klein, Temple University, Philadelphia, PA, and approved March 5, 2020 (received for review October 15, 2019)

We report here the pressure-induced amorphization and reversible structural transformation between two amorphous forms of SO_2: molecular amorphous and polymeric amorphous, with the transition found at 26 GPa over a broad temperature regime, 77 K to 300 K. The transformation was observed by both Raman spectroscopy and X-ray diffraction in a diamond anvil cell. The results were corroborated by ab initio molecular dynamics simulations, where both forward and reverse transitions were detected, opening a window to detailed analysis of the respective local structures. The high-pressure polymeric amorphous form was found to consist mainly of disordered polymeric chains made of three-coordinated sulfur atoms connected via oxygen atoms, with few residual intact molecules. This study provides an example of polyamorphism in a system consisting of simple molecules with multiple bonds.

polyamorphism | sulfur dioxide | high pressure | polymeric form

Polyamorphism is the counterpart of polymorphism observed in crystalline solids. It is characterized by the existence of two or more disordered forms, either amorphous or liquid, differing in local structural order while preserving the stoichiometry. This phenomenon is often also accompanied by changes in coordination and density (1, 2) (for recent reviews, see refs. 3 and 4). Transformations between these different amorphous forms can be driven by pressure and temperature. While, in the case of crystalline polymorphs, the structural transitions are often (at least in principle) of first order and sharp, transitions in amorphous systems occur between isotropic forms and are more likely to be continuous. This is related to the absence of constraints prescribed by lattice periodicity, allowing for a gradual transformation between very different forms.

The first and perhaps most celebrated example of polyamorphic behavior was discovered in water ice in 1984 by Mishima et al. (5, 6), observing that compression of ice I_h at 77 K induced a transformation to an amorphous state. Through specific compression/decompression/heating protocols, at least two different forms of amorphous water ice were identified, known as low-density amorphous (LDA) and high-density amorphous (HDA) ices. The local structural order in the HDA and LDA ices differs by the presence of non–hydrogen-bonded water molecules in the first coordination shell of the former, resulting in the two forms having substantially different density. The existence of two amorphous forms of water ice was suggested to be related to existence of liquid–liquid transition and a second critical point of water (7).

Similar phenomena have also been observed in other important systems such as Si (8), SiO_2 (9–11), and GeO_2 (12), where the polyamorphism is related to a change from tetrahedral to octahedral coordination at high pressure. Other examples where pressure induces changes in simple molecular systems include amorphous S (13) and liquid S (14) (for more examples and review, see refs. 3 and 4). Dramatic structural changes leading to amorphization have been observed upon compression of molecular crystals where multiple bonds are present. It is well known that pressure can destabilize multiple bonds in molecules in favor of extended polymeric networks with a higher coordination. Due to the associated strong kinetic effects, creation of amorphous forms is often observed, especially when compression is performed at low temperatures. Amorphization of molecular crystals at high pressure has been observed in the famous examples of nitrogen (15, 16), carbon dioxide (17, 18), and benzene (19–21). In nitrogen, the strong triple bond of the molecule breaks under high pressures, giving rise to a single-bonded network. In carbon dioxide, the double bond becomes unstable, and carbon coordination increases to three and four. In the case of benzene, the aromatic ring opens, and a network of hydrogenated carbons with single bonds is formed. The parent crystalline states of these amorphous materials have been

Significance

Some substances are known to exist in several different structurally disordered solid states and transform between them similarly to structural phase transitions between crystalline polymorphs. This interesting and yet not fully understood phenomenon is called polyamorphism, and notable examples include water, SiO_2, Si, etc. Here we present an example of such behavior in a simple molecular substance, SO_2. By using experimental high-pressure techniques, we observe a reversible transition between different amorphous states around 26 GPa. Experimental results are well supported by ab initio simulations, which identify the high-pressure amorphous form as a nonmolecular, polymeric one consisting of intertwined chains. Our findings contribute to the fundamental understanding of structure of disordered matter as well as high-pressure behavior of simple archetypal molecules.

Author contributions: M.S., F.A.G., and R.M. designed research; H.Z., O.T., and F.A.G. performed research; H.Z., O.T., S.D.P., M.S., F.A.G., and R.M. analyzed data; O.T., X.-D.L., R.B., E.G., P.D.-S., S.D.P., M.S., F.A.G., and R.M. wrote the paper; and X.-D.L., R.B., E.G., P.D.-S., and S.D.P. contributed to the discussion of results.

The authors declare no competing interest.

This article is a PNAS Direct Submission.

[1]To whom correspondence may be addressed. Email: gorelli@lens.unifi.it, xiaodi@issp.ac.cn, santoro@lens.unifi.it, or martonak@fmph.uniba.sk.

This article contains supporting information online at https://www.pnas.org/lookup/suppl/doi:10.1073/pnas.1917749117/-/DCSupplemental.

First published April 3, 2020.

discovered both in nitrogen (22, 23) and in carbon dioxide (24, 25) after high-temperature annealing obtained by means of laser heating.

Experiments

Sulfur dioxide is an important molecule in chemistry, serves a significant role in industrial applications, and has been attributed to atmospheric and geological processes. Unlike CO_2, the SO_2 molecule is bent, described by two resonant structures with one single and one double bond (26, 27). The crystalline forms of SO_2 have been previously experimentally studied at pressures up to 32 GPa, by Song et al. (28). Here, we present a combined experimental and computational study of SO_2 up to pressures of 60 GPa and over a broad temperature regime. Observations via Raman spectroscopy and X-ray diffraction (XRD), well supported by ab initio simulations, provide a detailed description, on the atomistic level, of the transformations under compression/decompression cycles. These findings give evidence of a hitherto unobserved example of polyamorphism related to a reversible transformation between molecular and polymeric amorphous forms of SO_2.

Raman Spectroscopy

In Fig. 1, we present a selection of Raman spectra measured upon increasing pressure up to 60 GPa, at 77 K (Fig. 1*A*), as well as subsequent decompression back to ambient pressure at room temperature (Fig. 1*B*). Similar experiments for compressions at 210 K were also conducted and are reported in *SI Appendix*, Fig. S1. We find, in general, an agreement between our Raman measurements of solid molecular SO_2 under pressure and those reported previously (28). However, the dramatic spectral changes at low temperatures were not observed previously, as pressures were limited to only 22 GPa (28). From these datasets, what is readily evident is the progression from sharp molecular peaks of SO_2, that is, ν_1 1,050 cm^{-1} to 1,220 cm^{-1}, ν_3 1,240 cm^{-1} to 1,320 cm^{-1}, and ν_2 520 cm^{-1} to 600 cm^{-1}, to much broader, weaker peaks upon compression. In addition, new broad and weak bands appear at different frequencies, characteristics which are compatible with pressure-induced amorphization together with major changes in the local structure. Further, the well-defined molecular peaks of SO_2 are recovered upon decreasing pressure, while the new broad bands resulting from symmetry loss disappear, demonstrating that these changes are, indeed, reversible and are therefore incompatible with any irreversible processes, such as chemical decomposition ($SO_2 \rightarrow S + O_2$).

Taking a detailed analysis of the spectra, we can shed light on a number of remarkable features. We find that the numerous sharp lattice peaks, observed below 300 cm^{-1} to 400 cm^{-1}, weaken above 16 GPa (or above 10 GPa at 210 K; *SI Appendix*, Fig. S1) until they become undetectable above 21 GPa at 77 K (Fig. 1*A*) (or above 22 GPa at 210 K; *SI Appendix*, Fig. S1), and instead are replaced by a new broad band in the same spectral region. However, at higher frequencies, under the same conditions, we do not observe any additional peaks other than the molecular peaks, ν_1, ν_2, and ν_3, of SO_2 up to 25 GPa. The linewidth of the crystal peaks severely increases upon growing pressure, while the intensity decreases substantially. These spectral changes are highly indicative that, upon cold compression above 10 GPa to 15 GPa, crystalline molecular SO_2 undergoes a structural transformation into an amorphous form while preserving its molecularity, that is, consisting of SO_2 molecular units. Amorphization could have been enhanced by the shear stress, which is, in turn, related to the deformation of the gasket hole. This is supported also by our density functional theory (DFT) calculations (*Ab Initio MD Simulations*). Upon further compression, above 22 GPa to 25 GPa, additional and significant modifications to the Raman signature are observed; the ν_2 and ν_3 peaks progressively diminish and are barely observable above 30 GPa to 34 GPa. Conversely, the strongest Raman excitation of SO_2, ν_1 (1,170 cm^{-1} to 1,200 cm^{-1} [Fig. 1*A*]), is visible to the maximum pressures of 50 GPa to 60 GPa (see also Fig. 1*B*), albeit comparatively weaker. The ν_1 band peak is found to merge with an altogether new weak and broad peak centered at 1,220 cm^{-1} to 1,230 cm^{-1}, denoted as α in Fig. 1*A*. In addition to emergence of the α-peak, another new and broad band appears at 600 cm^{-1} to 1,000 cm^{-1} with a high-frequency edge at around 900 cm^{-1}, which we call β. Both bands α and β appear to be of nonmolecular origin, which suggests that the emergence of these excitations signals that amorphous-molecular SO_2 undergoes a transformation into a nonmolecular/extended amorphous form.

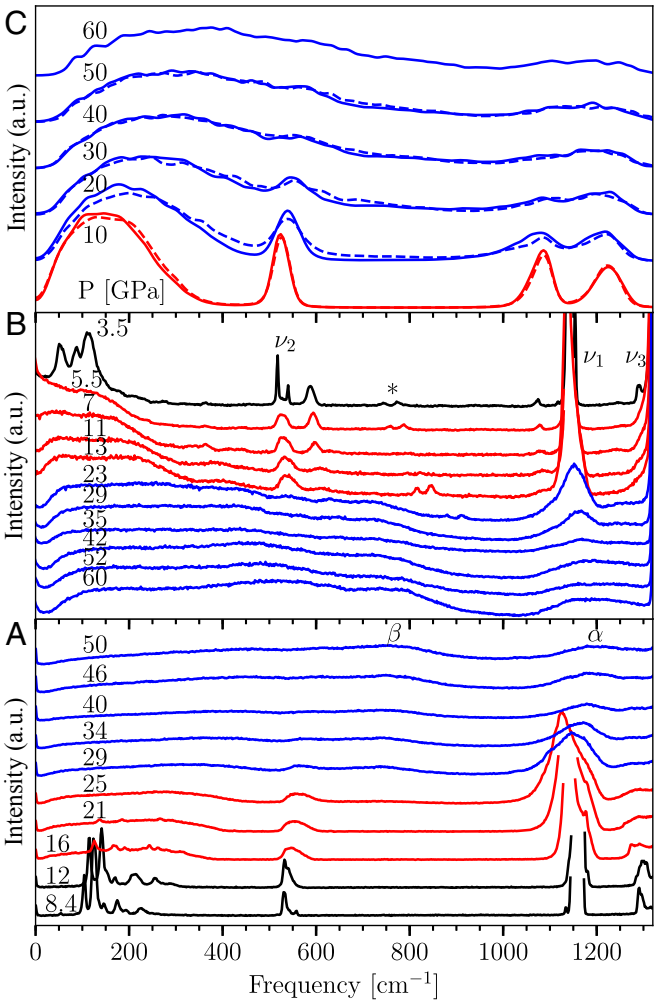

Fig. 1. Vibrational spectra of solid SO_2. (*A* and *B*) Selected Raman spectra of an SO_2 sample measured upon (*A*) increasing pressure at 77 K and (*B*) decreasing pressure at room temperature. During compression, the initially sharp molecular peaks of SO_2, ν_1, ν_2, and ν_3, broaden and become very weak, while new broad and weak bands appear at different frequencies, indicating pressure-induced amorphization together with changes in the local structure. Upon decompression, the sharp molecular peaks of SO_2, ν_1, ν_2, and ν_3, are recovered, while the new broad bands disappear at the same time, showing that amorphization and overall changes in the local structure are reversible. (*C*) Evolution of VDOS from ab initio MD simulations along compression (solid lines) and decompression (dashed lines) at $T = 300$ K. Color represents structural state of the system: black, molecular crystal; red, molecular amorphous; blue, polymeric amorphous. Star in *B* marks ruby peaks.

Comparison with the pressure-induced molecular to amorphous-nonmolecular transformation in CO_2 (17, 18, 25) can help to interpret the transformation observed here in SO_2, as it bears similarities. Carbonia, the nonmolecular amorphous CO_2, has been shown to be made of a mixture of C in a threefold and fourfold oxygen coordination in similar proportions. The threefold coordinated C sites are uniquely identified by C=O stretching peaks in the Raman and the infrared (IR) spectrum, 1,900 cm^{-1} to 2,000 cm^{-1} at 50 GPa to 60 GPa, which roughly corresponds to the average value, ν(stretch CO_2), between the symmetric and the antisymmetric stretching modes of molecular CO_2. However, when considering the full Raman and IR spectra, the single C–O bond stretching and deformation modes ascribed to both threefold and fourfold coordinated C sites form a broad spectral distribution extending over 500 cm^{-1} to 1,500 cm^{-1}, ∼0.26 to 0.77 of the average ν(stretch CO_2). Consequently, in the case of SO_2, the aforementioned peak, α, is roughly the average frequency of the two molecular stretching modes, and can therefore be attributed to the S=O stretching modes for nonmolecular/extended SO_2 with S in threefold coordination by O. In addition, in the frequency range given by 0.26 to 0.77 of α, 320 cm^{-1} to 940 cm^{-1}, we observe the previously described band β. Therefore, again in accordance with the CO_2 analogue, the β band can be attributed to single S–O bond stretching and deformation modes in the nonmolecular/extended SO_2. A discrepancy of using carbonia as an analogue, however, is that the fourfold oxygen coordination is absent in SO_2, in accordance with our DFT simulations (discussed later). We do, however, also have a two-component system, considering that the ν_1 peak for molecular SO_2 is still present at the highest pressures, although weak. Therefore, we infer that the overall nonmolecular/extended SO_2 consists of a mixture of trace twofold S sites, still molecular in nature, in a bulk of nonmolecular threefold coordinated S sites. An alternative possibility compatible with experimental data would be that molecular parts of the sample with twofold coordinated S and nonmolecular parts with S in higher coordination are phase-separated on a macroscopic/mesoscopic scale.

On decompression, the spectral changes and transformations identified previously on compression are reverted, as shown in Fig. 1*B*. However, a minor hysteresis is observed, attributed to the kinetically limited structural changes. We observe that, when the sample is decompressed below 30 GPa to 25 GPa, both the α peak and β band disappear, while the well-defined molecular peaks ν_1, ν_2, and ν_3 emerge suddenly. Further, in the low-frequency/lattice region below 350 cm^{-1}, a diffuse, liquid-like band clearly develops, with no additional substantial changes down to about 5 GPa. These changes demonstrate again a change in the amorphous structure, recovering molecular SO_2 units at 25 GPa to 5 GPa on decompression. This molecular amorphous form is then found to further transform into a crystalline molecular SO_2 structure below 5 GPa, indicated by the sharp lattice mode peaks observed below this pressure and crystalline XRD (discussed later). Interestingly, an additional peak is found below 20 GPa at around 600 cm^{-1} which was also observed in a previous study, where it was attributed to the formation of molecular clusters (28). The reversible transformations of SO_2 to molecular and nonmolecular amorphous forms again parallel the similar case of CO_2 (17, 18, 25), and are at odds with the cases of aromatic molecules, where, instead, amorphous nonmolecular forms obtained at high pressures are recoverable to ambient conditions (19–21, 29, 30).

XRD

The noncrystalline nature of SO_2 at high pressure has also been assessed by XRD, and the evolution of the static structure factor upon room-temperature decompression of sample compressed at low temperature is shown in Fig. 2*A*. The static structure factor has been obtained by the empty cell subtraction, taking into account the form factors of oxygen and sulfur as well as the Compton contribution from the sample, following a procedure described elsewhere (31). In general, it is found that, at the highest pressures, the two peaks at about 2.2 and 3 $Å^{-1}$ are of similar intensity, while, on decompression, the first peak significantly increases with respect to the second one, which, at the same time, moves to lower Q. The comparison between the patterns measured at 35.5 GPa and 23.5 GPa shows a clear change of the static structure factor. The first contribution, centered at 2.2 $Å^{-1}$, becomes more prominent and sharpens markedly, while the second has a more subtle loss of intensity. These changes, corresponding to the transformation from an extended amorphous to a molecular amorphous form, are in strong agreement with the Raman results outlined previously.

Furthermore, similarly to what was observed in the Raman experiments, at the lowest pressures, the molecular amorphous

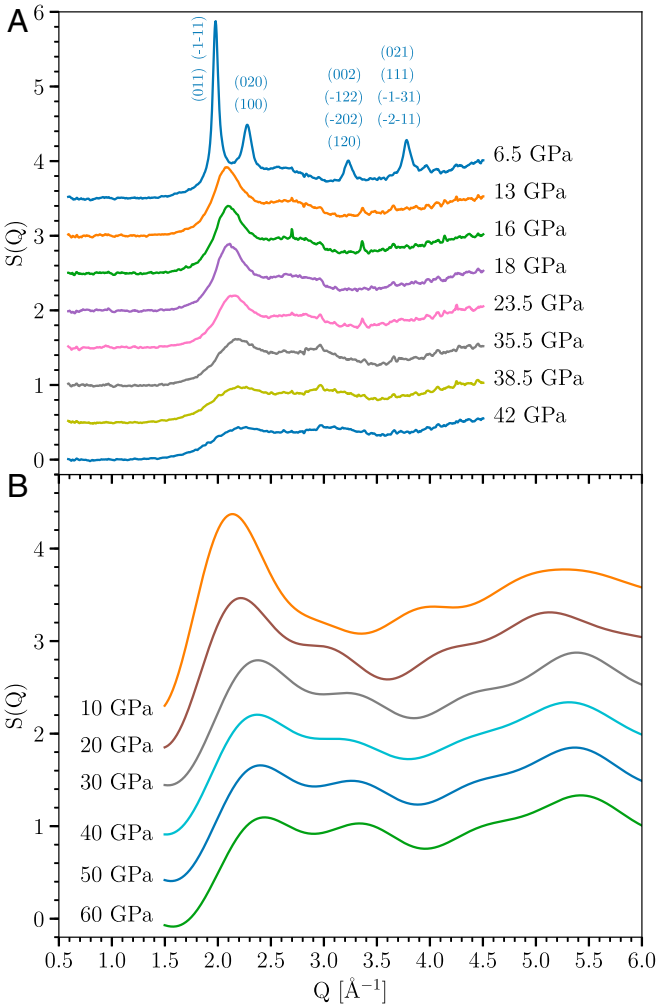

Fig. 2. Static structure factor of solid SO_2 under pressure. (*A*) Experimental *S*(*Q*) measured along a room-temperature decompression run. (*B*) *S*(*Q*) computed from simulations at 300 K during decompression (the graph computed from simulation of compression is in *SI Appendix*, Fig. S2). Region of *S*(*Q*) beyond 4.5 $Å^{-1}$ in *A* is inaccessible because of limited angle in experiment, while the region below 1.5 $Å^{-1}$ in *B* is not reliable because of limited RDF range, resulting from the simulation supercell size of 14 Å. The Bragg peaks at 6.5 GPa in *A* have been partially indexed on the basis of an *Aea2* space group with a = 5.5430 Å, b = 5.4011 Å, and c = 5.5356 Å as obtained from simulations (see also *SI Appendix*, Fig. S11).

form is found to start transforming into a crystalline molecular SO_2 structure at about 6.5 GPa. The observed Bragg peaks can be partially assigned on the basis of the *Aea2* structure (experimentally found at ambient pressure) compressed to 6.5 GPa (see also *SI Appendix*, Fig. S11 and *Evolutionary Crystal Structure Prediction*).

Summary of Experimental Observations

In summary, we have observed two distinct structural transformations: at lower pressures, the transformation from a molecular crystal to a molecular, van der Waals-type, amorphous solid, with no changes in the molecular unit, and to a nonmolecular/extended state on further compression. Interestingly, a substantial effect of temperature is observed for the former transformation, despite expecting the energy barrier to be comparatively small. For example, instead of an expected isobaric phase line, the transformation occurs at 5-GPa-lower pressures at 210 K compared with 77 K isotherm. Conversely, the second transformation, to a nonmolecular/extended amorphous state, is a chemically reconstructive one, and therefore would logically have a higher associated energy barrier and consequently a stronger temperature dependence. Instead, this transformation is observed at roughly the same pressures for both isotherms studied, 77 K and 210 K, at around 25 GPa to 30 GPa, counterintuitively suggesting that the barrier for polymerization is small in relation to the one for the initial molecular amorphization. We note that this is quite different from the case of CO_2 and N_2, where a much stronger hysteresis is reported (23–25).

Ab Initio Molecular Dynamics Simulations

In order to obtain a better understanding of the processes on an atomistic level, we performed ab initio molecular dynamics (MD) simulations following a pressure path akin to the experiment. We first performed a test in order to check whether applying shear stress to a perfect *Aea2* molecular crystal at low pressure might result in amorphous molecular structure as observed in experiments. We gradually induced shear strain by deforming the γ-angle of the supercell by up to 30° and observed transformation into a disordered molecular form, confirming the experimentally observed amorphization.

The full simulation protocol is shown in *SI Appendix*, Fig. S3. In order to start the compression from a well-defined amorphous molecular structure, we melted a perfect *Aea2* molecular crystal (32) in a $3 \times 3 \times 3$ supercell (108 SO_2 molecules, equivalent to a 324-atom unit cell) by heating at $P = 0$ GPa to 600 K. Through subsequent cooling to 0 K, we prepared the amorphous structure, which served as an initial configuration for further simulations. Following the experimental pathway, we performed a gradual compression to 60 GPa and subsequent decompression to 10 GPa (in 10-GPa steps) at 300 K in order to accelerate the structural transformations (both on compression and decompression). Interestingly, at this temperature, we observed some diffusion of molecules in the molecular phase, suggesting that the sample might possibly be in metastable liquid state.

Analysis of the partial radial distribution functions (RDFs) (Fig. 3), obtained from simulations, can provide a more detailed description of the observed transformations on an atomistic level. The RDFs clearly indicate the reversible amorphous to amorphous transformation, corresponding to the S in twofold to threefold O coordination change, providing further evidence for the experimentally observed forms and their associated reversibility. Upon compression of the initial molecular amorphous sample to 10 GPa at 300 K, SO_2 retains its molecular units. Evidenced in Fig. 3*A*, the peak at 1.44 Å, corresponding to the double bond, is sharp and well separated from the next neighbor at 2.5 Å to 3.0 Å and the coordination number of S

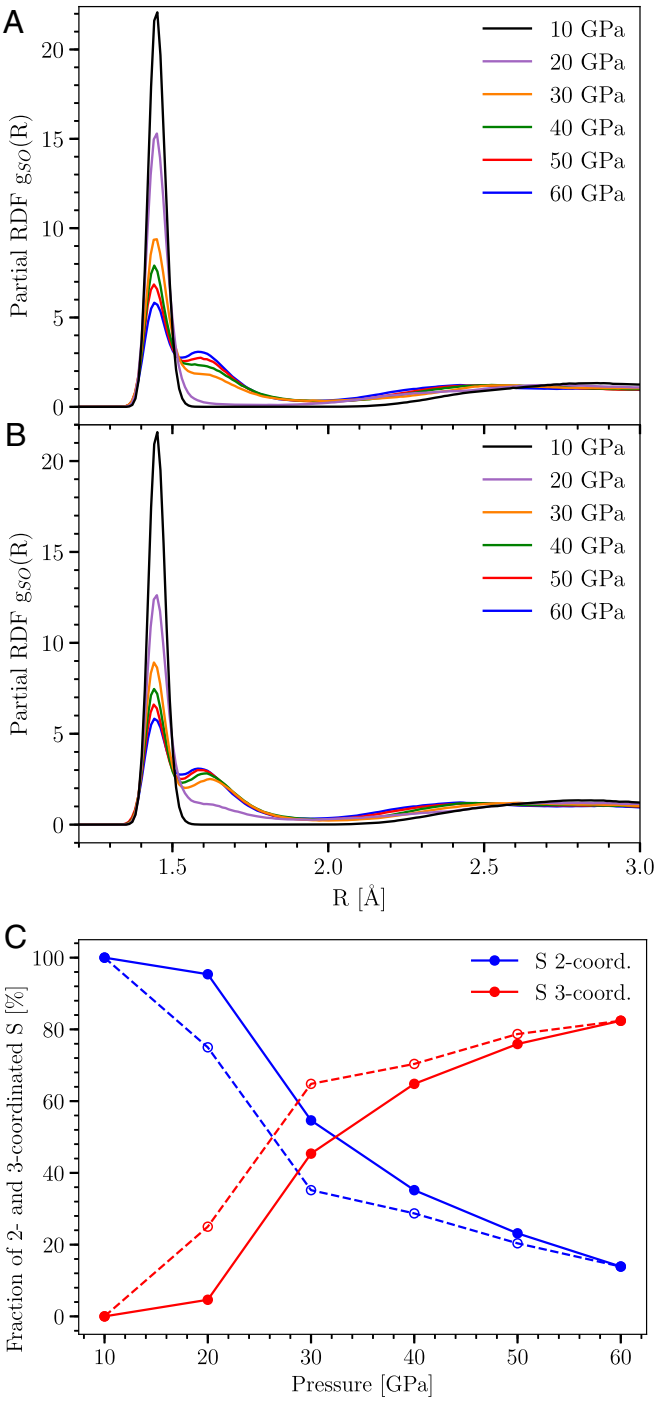

Fig. 3. Partial S–O RDF [g_{SO}(R)] and concentration of sulfur coordination states at different pressures from MD simulations at 300 K. (*A*) RDF during compression, (*B*) RDF during decompression, and (*C*) fraction of two- and three-coordinated S atoms during compression (solid line) and decompression (dashed line). Coordination number was determined within the cutoff of 1.92 Å.

atoms with respect to O atoms is 2. Upon compression to 20 GPa, modifications in the RDF are observed, and, at 30 GPa, there is a substantial change: The first peak becomes weaker while a new peak at slightly longer distance, 1.6 Å, appears. These changes indicate that some of the S=O double bonds are broken and replaced by single ones. In the same pressure regime, three-coordinated S atoms appear with two single S–O bonds

and one S=O double bond, forming polymeric chains (see snapshots shown in Fig. 4). On further compression, the first peak is found to progressively diminish in intensity while the second is enhanced, resulting in 82% of S atoms being in threefold oxygen coordination at 60 GPa. On decompression (Fig. 3*B*), akin to experimental observations, we observed the reverse evolution, further demonstrated by the pressure dependence of the number of two- and three-coordinated S atoms in Fig. 3*C*. Additionally, at 10 GPa, the previously identified polymeric chains observed on compression disappear entirely (Fig. 4), and the system reverts back to its initial molecular amorphous state. The strong agreement between experiment and simulations means that insights from the MD calculations can identify the experimental observations as forward and backward transitions between molecular and polymeric amorphous forms of SO_2. The dependence of the coordination number of S atoms on pressure (Fig. 3*C*) exhibits some hysteresis, which suggests that the transition might have a weakly first-order character. The pressure dependence of density upon compression and decompression, shown in *SI Appendix*, Fig. S4, shows a very small hysteresis and does not exhibit any particular features across the structural transformation. We performed a similar compression simulation also at 500 K and found the polymerization to start at 30 GPa, suggesting that the transition is shifted to higher pressure upon increasing temperature.

Above 20 GPa, the calculated static structure factor, $S(Q)$, shows important changes upon compression (*SI Appendix*, Fig. S2). The intensity of the first diffraction peak at about 2.2 $Å^{-1}$ drops, while a new peak appears, around 3 $Å^{-1}$, which grows with increasing pressure. At 60 GPa, the height of both peaks becomes similar, reflecting XRD patterns above 35.5 GPa in Fig. 2*A*. All changes are found to be reversible upon decompression, albeit with a small hysteresis, and the calculated structure factor agrees very well with the experimental one (Fig. 2). Simulations allow us to decompose the total $S(Q)$ into contributions from atomic pairs (*SI Appendix*, Fig. S5) The first peak, around 2.2 $Å^{-1}$, originates mainly from nonbonded S···S pairs, while the weaker second peak, at 3 $Å^{-1}$, comes from O···O, and, finally, the broad peak, around 5 $Å^{-1}$, is mainly due to the S–O pairs. It is clear that the loss of the first peak of total $S(Q)$ is a consequence of changes in the S–O contribution, which exhibits a pronounced drop above 20 GPa (*SI Appendix*, Fig. S5). Therefore, the observed evolution of $S(Q)$ directly reflects changes of the distance of S–O neighbors upon polymerization.

On compression, comparing the vibrational spectra from simulations (Fig. 1*C*) with experimental Raman spectra (Fig. 1*A*), we observe qualitatively similar evolution. Above 20 GPa, the distinct ν_2 peak at 550 cm^{-1} progressively disappears, while the 400 cm^{-1} to 500 cm^{-1} and 600 cm^{-1} to 900 cm^{-1} regions become enhanced. Meanwhile, the two molecular peaks, ν_1 around 1,100 cm^{-1} and ν_3 above 1,200 cm^{-1}, gradually merge into a single broad peak around 1,200 cm^{-1}, again in agreement with experiments (Fig. 1*A*). The evolution of the peaks can be understood from the projected vibrational density of states (VDOS), allowing decomposition of the total VDOS into contributions from structurally distinct S and O atoms (*SI Appendix*, Fig. S6). Both S and O atoms can be either in molecules or in polymeric chains. Moreover, O atoms in polymeric chains are either at a bridging position between two S atoms (S–O–S) or at the terminal position, doubly bonded to S atoms (S=O). The evolution of the total VDOS clearly reflects the gradual conversion of molecules into polymeric chains. Again, upon decompression, the reverse evolution is observed, in agreement with experiment (Fig. 1*B*).

Evolutionary Crystal Structure Prediction

In order to understand the origin of the two amorphous forms, it is useful to discuss their underlying crystalline counterparts. SO_2 forms at ambient pressure and low temperature below 201 K, an *Aea2* molecular crystal (32). Conversely, its analogue SeO_2 forms, at ambient pressure, a $P4_2/mbc$ polymeric crystal consisting of chains [mineral Downeyite (33)]. The possible existence of polymeric SO_2 (polysulfite) was studied in refs. 34 and 35, where energies of various oligomers were calculated. Additionally, in ref. 35, a crystal structure with infinite polymeric chains was studied, obtained by substituting Se atoms in Downeyite by S atoms. It was concluded that polymeric SO_2 is energetically higher than its molecular form, and it was proposed that the polymer could be stabilized at high pressure. Quantitatively, the energy difference between polymeric and molecular forms was found to be −19.7 kcal/mol for SeO_2 and 5.5 kcal/mol for SO_2 (table 1 in ref. 35). This can be understood by applying the well-known pressure homology rule (36–38) stating that light elements behave at high pressure like heavier elements from the same group at lower pressures.

The structure of crystalline polymeric phases of SO_2 has not been, to our knowledge, determined experimentally. In order to check their possible existence at high pressure, we performed a structural search of crystalline phases of SO_2, employing an

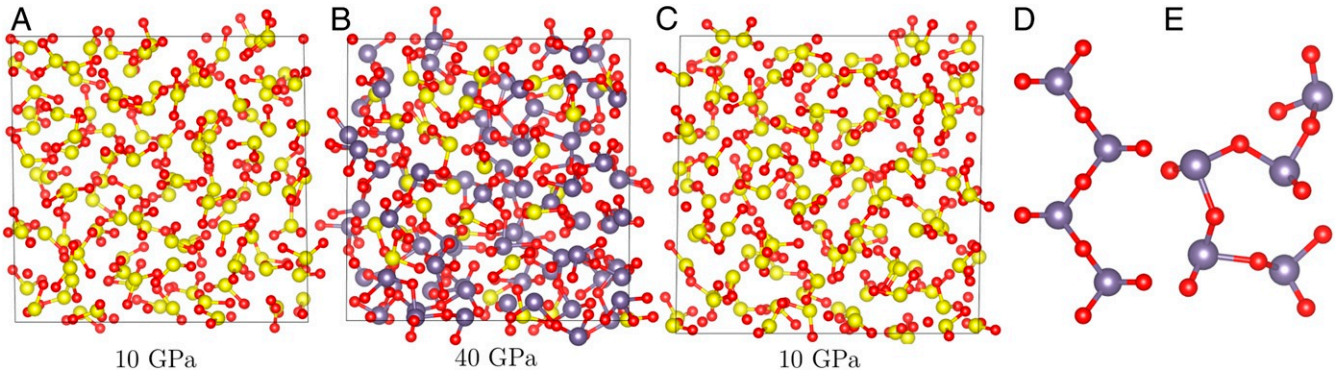

Fig. 4. (*A*–*C*) Snapshots of the amorphous sample from MD simulations at different pressures. (*A*) The beginning of compression at 10 GPa where the sample consists only of SO_2 molecules. (*B*) Structure during compression at 40 GPa where the sample contains both molecules and polymeric chains. (*C*) Structure after decompression to 10 GPa where the sample reverted from polymeric back to molecular. Simulation supercells are not to scale. (*D* and *E*) Comparison of polymeric chains in crystalline and amorphous forms of SO_2. (*D*) Chains in crystalline *Ama2* and $Pmc2_1$ phases. (*E*) Selected disordered chain in a configuration of a-SO_2 from MD simulation at 30 GPa. The color of S atoms represents coordination: two-coordinated atoms (molecule) are yellow, and three-coordinated ones (polymeric chains) are blue-gray.

evolutionary approach (details are described in *Materials and Methods*). We show here the main results of our search. The enthalpy vs. pressure graph for low-enthalpy phases is shown in *SI Appendix*, Fig. S7. At zero pressure, we found the lowest enthalpy for the molecular crystal structure with space group *Aea2*, in agreement with experiment (32). Upon increasing pressure, we found another molecular crystal structure $P2_1/c$ which becomes stable above 1 GPa. Besides this structure, there are two low-lying metastable molecular structures, *Pc* and *Cc*, which, upon further compression, transform into polymeric structures. The molecular *Cc* structure spontaneously transforms to polymeric *Ama2* phase beyond 13 GPa (reaching limit of dynamical stability), and, in the same manner, molecular *Pc* phase transforms beyond 17 GPa into polymeric $Pmc2_1$ phase (all structures are shown in *SI Appendix*, Fig. S8, and cif files of the *Pc*, *Cc*, $Pmc2_1$, and *Ama2* structures are included in *SI Appendix*). Both polymeric structures have very similar enthalpy and become thermodynamically stable with respect to the molecular phases already at 11 GPa. They also have the same conformation of chains and differ only in chain stacking. The mechanism of polymerization is illustrated in *SI Appendix*, Fig. S9, showing the pressure evolution of bond lengths upon compression. A similar polymerization mechanism is likely to apply also in the amorphous form when molecules of suitable orientation approach each other (see also *Connection between Crystalline and Amorphous Forms*). Both polymeric structures have the same conformation of chains as SeO_2 Downeyite, but the stacking of chains is different. The stable polymeric structure has, at 20 GPa, a bond length of 1.46 Å between S atom and terminal oxygen (S=O) and 1.65 Å between S atom and bridging oxygen (S–O), similar to the peak positions of S–O RDF (Fig. 3). The sulfur atom in the chain is surrounded by three oxygen atoms in roughly trigonal pyramid coordination (at 20 GPa, bond angle O–S–O is 90° and O=S–O is 100°), suggesting the presence of sp^3 hybridization (see also ref. 35, where it was suggested that the dimerization of SO_2 is related to $sp^2 \rightarrow sp^3$ rehybridization). In order to quantitatively assess the bond order of S–O bonds in molecular and polymeric SO_2, we employed the density driven electrostatic and chemical (DDEC6) atomic population analysis method (39). We found a bond order of 2.12 in molecule and 2.14 and 1.15 for S=O and S–O bonds in the polymeric phase. In *SI Appendix*, Fig. S10, we show the electronic density of states including projections on *s* and *p* orbitals for the crystalline molecular *Cc* and polymeric *Ama2* phase (no *d*-orbital participation was found). We also note that the diffraction pattern of the recrystallized phase upon decompression to 6.5 GPa (Fig. 2*A*) shows a strong similarity to the diffraction pattern of the molecular phase *Aea2* at the same pressure (for comparison, see *SI Appendix*, Fig. S11). This provides additional evidence that the system after the compression/decompression cycle returns to its parent state.

Connection between Crystalline and Amorphous Forms

To make a connection to the polymeric amorphous form, we note that different molecular crystalline phases shown in *SI Appendix*, Fig. S7 have different limits of dynamical stability with respect to polymerization. While the $P2_1/c$ phase remains molecular even at 30 GPa, the phases *Cc* and *Pc* polymerize beyond 13 and 17 GPa, respectively (*SI Appendix*, Fig. S9). This points to the fact that the pressure threshold for polymerization depends on the relative orientation of molecules. In the amorphous form, where random relative orientations are present, polymerization needs a higher pressure beyond 20 GPa to start. In Fig. 4 *D* and *E*, we show a comparison of chains from crystalline polymeric phases $Pmc2_1$ and *Ama2* and selected disordered chain from the amorphous sample. It can be seen that the local environment is similar, except for the dihedral angles. While the crystalline forms have well-defined values (e.g., $O_{terminal}$–S–O_{bridge}–S angle around 136°), in the amorphous form, one can find nearly all values of the dihedral angles. We note that, in an early study (35), the effect of conformational changes on the energy of SO_2 oligomers was studied, and it was found that, in this respect, the potential energy surface is very soft. This rationalizes our observation of the variety of dihedral angles found in chains in the amorphous form.

To assess quantitatively the effects of structural disorder, we calculated the enthalpy of the amorphous form (relaxed to $T = 0$) and found it, at 10 GPa, to be about 0.26 eV per formula unit above the crystalline phases (it is shown in *SI Appendix*, Fig. S7). Above 20 GPa, where the transition starts, the curve changes slope, and goes down, but much slower than the crystalline polymeric phases, because of incomplete polymerization in the amorphous form. We note that, because of the short time scale available in the ab initio MD simulations (of the order of 10 ps), the amorphous structure might not be fully relaxed structurally. We also determined, with our DFT simulations, the electronic properties of the a-SO_2 phase and found that the system does not metalize up to 60 GPa, having a band gap (in the Perdew–Burke–Ernzerhof [PBE] approximation) of at least 0.6 eV.

Conclusions

We observed a pressure-induced amorphization and a reversible structural transition between molecular and polymeric amorphous forms of SO_2 at pressures around 26 GPa. The transition has small hysteresis, pointing to the fact that the associated kinetic barriers are low. The lower pressure of the transition between molecular and polymeric amorphous forms, as well as the back-transformation, is qualitatively facilitated by the molecular polarity. This, supported by the high density attainable under pressure, drives the intermolecular interaction and lowers the activation energy of the transformation. To our knowledge this kind of transition was not previously observed and provides an example of reversible structural transition between disordered nonequilibrium states of solid matter. Unlike in a-CO_2, where polymeric a-carbonia contains three- as well as four-coordinated C atoms, here the molecular form converts into polymeric form with only three-coordinated S atoms. It will be of interest to study whether the two structurally distinct forms continue to exist also in liquid state, either in stable or metastable (supercooled) regions. For example, a transition between molecular and polymeric liquid has been proposed in nitrogen (40), and a cross-over between such forms was observed in recent computational study of amorphous nitrogen (41). Further experimental and theoretical work is necessary to accurately map the solid and liquid regions and uncover further details of the phase diagram of SO_2.

Materials and Methods

Experimental Methodology. The SO_2 gas was loaded into the diamond anvil cell (DAC) by means of cryogenic loading: The gas was condensed between one diamond anvil and the gasket placed on the other diamond of a DAC, which was opened by a few millimeters and cooled to liquid nitrogen temperature inside a sealed glove box purged with nitrogen to avoid moisture condensation. We performed Raman spectroscopy using a state-of-the-art confocal Raman microscope with 15 and 2 μm of axial and transverse resolution, respectively. The spectrometer consisted of a Spectra Pro 750-mm monochromator, equipped with a Pixis Princeton Instrument charge-coupled device detector. Bragg grate filters were used to attenuate the laser light and spatial filtering of the collected light to obtain high-quality spectra down to 7 cm^{-1} with minimal background from the diamond anvils and strong signal from the sample. The laser beam was expanded and cleaned by a band-pass filter. We used a Laser Torus at 660 nm with 10 mW of power and Laser Ventus at 532 nm with 0.5 mW of power to check for the presence of eventual fluorescence bands in the spectrum. We generally used a 300-grooves-per-mm grating, as the spectral features were getting very broad and weak with pressure. The pressure was determined by the fluorescence of a small

ruby placed in the sample or from the stressed part of the diamond anvil, which we detect with high accuracy thanks to the excellent spatial resolution of the setup. The XRD measurements were made at Petra (proposal ID: I-20181128) using a monochromatic X-ray beam with 42.7-keV energy ($\lambda = 0.2922$ Å), and the scattered X-rays were detected by a PerkinElmer XRD1621 (2,048 × 2,048 pixels, 200 × 200 μm^2) detector. The diffraction patterns have been measured only along decompression of an amorphous sample obtained from a compression at low temperature while monitoring the changes with Raman spectroscopy. The excellent transverse spatial resolution allows us to obtain clean diffraction patterns of the sample without the presence of spurious diffraction lines from the metallic gasket. The empty cell subtraction, which is of fundamental importance to obtain reliable measurements of the diffuse scattering from an amorphous or liquid sample in the DAC, has been, in this case, easily obtained by measuring the empty cell at the end of the decompression run when the SO_2 has completely back-transformed to the gas state and escaped from the sample chamber.

Simulations Methodology. We performed a structural search for crystalline phases of SO_2 employing the USPEX (42) package at pressures of 10, 20, and 50 GPa with four formula units (12 atoms) within a unit cell. Ab initio simulations were performed by DFT as implemented in VASP 5.3 and 5.4 codes (43–45), employing projector augmented wave pseudopotentials (with six valence electrons for both S and O atoms) and PBE (46) parametrization of the generalized gradient approximation exchange–correlation functional. In evolutionary search, structural relaxations, and enthalpy calculations, we employed the harder S_h and O_h pseudopotentials with a cutoff of 910 eV, while, in MD calculations, we used the regular ones S and O with a cutoff of 520 eV. Compression, decompression, and heating were performed by 6-ps variable-cell isothermal-isobaric (NpT) simulations with Langevin thermostat and Γ-point Brillouin zone sampling. We used a time step of 2 fs and friction coefficients of 10.0 and 2.0 ps^{-1} for atomic and lattice degrees of freedom, respectively, and 10,000 m_u as barostat fictitious mass. Data for velocity autocorrelation function were generated by equilibrating a sample for 6 ps in NpT and then running 20-ps constant-volume microcanonical (NVE) simulation. Total and projected VDOS were computed in the standard way as Fourier transform of mass-weighted velocity autocorrelation function from MD trajectories at pressures from 10 GPa to 60 GPa. Static structure factors $S(Q)$ were calculated by performing Fourier transform of the RDFs from MD trajectories at several pressures along compression and decompression runs. All data referred to in the manuscript are available in the article and in *SI Appendix*.

ACKNOWLEDGMENTS. Experimental section of research was supported by the Chinese Academy of Sciences President's International Fellowship Initiative Fund (2018VMA0053 and 2019VMA0027), National Natural Science Foundation of China Grant (11874361, 51672279, 11774354, and 51727806), Chinese Academy of Sciences Innovation Grant (CXJJ-19-B08), Science Challenge Project (TZ2016001), and the Hefei Institutes of Physical Science Chinese Academy of Sciences Director's Fund Grant (YZJJ2017705). R.M. acknowledges stimulating discussions with P. Mach. R.M. and O.T. were supported by the Slovak Research and Development Agency under Contract APVV-15-0496. Calculations were performed at the Computing Center of the Slovak Academy of Sciences using the supercomputing infrastructure acquired in ITMS Projects 26230120002 and 26210120002 (Slovak Infrastructure for High-Performance Computing) supported by the Research and Development Operational Program funded by the European Regional Development Fund.

1. P. H. Poole, T. T. Grande, C. A. Angell, P. F. McMillan, Polymorphic phase transitions in liquids and glasses. *Science* **275**, 322–323 (1997).
2. P. F. McMillan, Polyamorphic transformations in liquids and glasses. *J. Mater. Chem.* **14**, 1506–1512 (2004).
3. D. Machon, F. Meersman, M. Wilding, M. Wilson, P. McMillan, Pressure-induced amorphization and polyamorphism: Inorganic and biochemical systems. *Prog. Mater. Sci.* **61**, 216–282 (2014).
4. M. A. Anisimov *et al.*, Thermodynamics of fluid polyamorphism. *Phys. Rev. X* **8**, 011004 (2018).
5. O. Mishima, L. D. Calvert, E. Whalley, 'Melting ice' I at 77 k and 10 kbar: A new method of making amorphous solids. *Nature* **310**, 393–395 (1984).
6. O. Mishima, L. D. Calvert, E. Whalley, An apparently first-order transition between two amorphous phases of ice induced by pressure. *Nature* **314**, 76–78 (1985).
7. P. H. Poole, F. Sciortino, U. Essmann, H. E. Stanley, Phase behaviour of metastable water. *Nature* **360**, 324–328 (1992).
8. P. F. McMillan, M. Wilson, D. Daisenberger, D. Machon, A density-driven phase transition between semiconducting and metallic polyamorphs of silicon. *Nature* **4**, 680–684 (2005).
9. M. Grimsditch, Polymorphism in amorphous SiO_2. *Phys. Rev. Lett.* **52**, 2379–2381 (1984).
10. R. J. Hemley, A. P. Jephcoat, H. K. Mao, L. C. Ming, M. H. Manghnani, Pressure-induced amorphization of crystalline silica. *Nature* **334**, 52–54 (1988).
11. Q. Williams, R. Jeanloz, Spectroscopic evidence for pressure-induced coordination changes in silicate glasses and melts. *Science* **239**, 902–905 (1988).
12. D. J. Durben, G. H. Wolf, Raman spectroscopic study of the pressure-induced coordination change in geo_2 glass. *Phys. Rev. B* **43**, 2355–2363 (1991).
13. C. Sanloup, E. Gregoryanz, O. Degtyareva, M. Hanfland, Structural transition in compressed amorphous sulfur. *Phys. Rev. Lett.* **100**, 075701 (2008).
14. L. Henry *et al.*, A density-driven first-order phase transition in liquid sulfur. arXiv:1709.09996 (28 September 2017).
15. A. F. Goncharov, E. Gregoryanz, H. Mao, Z. Liu, R. Hemley, Optical evidence for a nonmolecular phase of nitrogen above 150 GPa. *Phys. Rev. Lett.* **85**, 1262–1265 (2000).
16. E. Gregoryanz, A. F. Goncharov, R. Hemley, H. Mao, High-pressure amorphous nitrogen. *Phys. Rev. B* **64**, 052103 (2001).
17. M. Santoro *et al.*, Amorphous silica-like carbon dioxide. *Nature* **441**, 857–860 (2006).
18. J. A. Montoya, R Rousseau, M. Santoro, F. Gorelli, S. Scandolo, Mixed threefold and fourfold carbon coordination in compressed CO_2. *Phys. Rev. Lett.* **100**, 163002 (2008).
19. L. Ciabini, M. Santoro, R. Bini, V. Schettino, High pressure reactivity of solid benzene probed by infrared spectroscopy. *J. Chem. Phys.* **116**, 2928–2935 (2002).
20. L. Ciabini, M. Santoro, R. Bini, V. Schettino, High pressure photoinduced ring opening of benzene. *Phys. Rev. Lett.* **88**, 085505 (2002).
21. L. Ciabini *et al.*, Triggering dynamics of the high-pressure benzene amorphization. *Nature* **6**, 39–43 (2007).
22. C. Mailhiot, L. H. Yang, A. K. McMahan, Polymeric nitrogen. *Phys. Rev. B* **46**, 14419–14435 (1992).
23. M. I. Eremets, A. G. Gavriliuk, I. A. Trojan, D. A. Dzivenko, R. Boehler, Single-bonded cubic form of nitrogen. *Nature* **3**, 558–563 (2004).
24. F. Datchi, B. Mallick, A. Salamat, S. Ninet, Structure of polymeric carbon dioxide CO_2-**V**. *Phys. Rev. Lett.* **108**, 125701 (2012).
25. M. Santoro *et al.*, Partially collapsed cristobalite structure in the non molecular phase V in CO_2. *Proc. Natl. Acad. Sci. U.S.A.* **109**, 5176–5179 (2012).
26. J. E. House, *Inorganic Chemistry* (Academic, 2008).
27. T. Y. Takeshita, B. A. Lindquist, T. H. Dunning, Insights into the electronic structure of ozone and sulfur dioxide from generalized valence bond theory: Bonding in O^3 and SO^2. *J. Phys. Chem.* **119**, 7683–7694 (2015).
28. Y. Song, Z. Liu, H. Mao, R. J. Hemley, D. R. Herschbach, High-pressure vibrational spectroscopy of sulfur dioxide. *J. Chem. Phys.* **122**, 174511 (2005).
29. M. Ceppatelli, M. Santoro, R. Bini, V. Schettino, High pressure reactivity of solid furan probed by infrared and Raman spectroscopy. *J. Chem. Phys.* **118**, 1499–1506 (2003).
30. M. Santoro, M. Ceppatelli, R. Bini, V. Schettino, High-pressure photochemistry of furane crystal. *J. Chem. Phys.* **118**, 8321–8325 (2003).
31. J. H. Eggert, G. Weck, P. Loubeyre, M. Mezouar, Quantitative structure factor and density measurements of high-pressure fluids in diamond anvil cells by X-ray diffraction: Argon and water. *Phys. Rev. B* **65**, 174105 (2002).
32. B. Post, R. S. Schwartz, I. Fankuchen, The crystal structure of sulfur dioxide. *Acta Crystallogr.* **5**, 372–374 (1952).
33. K. Ståhl, J. P. Legros, J. Galy, The crystal structure of SeO2 at 139 and 286 K. *Z. für Kristallogr Cryst. Mater.* **202**, 99–108 (1994).
34. C. Groves, E. Lewars, Dimers, trimers and oligomers of sulfur oxides: an ab initio and density functional study. *J. Mol. Struct.* **530**, 265–279 (2000).
35. G. Frapper, Polysulfite, a hypothetical allotrope of sulfur dioxide? A molecular and periodic quantum investigation of covalent oligomeric and one-dimensional xo2-based compounds (X = S, Se). *New J. Chem.* **25**, 440–445 (2001).
36. R. Wentorf, "Chemistry at high pressures" in *The Physics and Chemistry of High Pressure* (Society of Chemical Industry, London, UK, 1963), vol. 1, pp. 185–190.
37. A. Neuhaus, Synthese, Strukturverhalten und Valenzzustände der anorganischen Materie im Bereich hoher und höchster Drucke. *Chimia* **18**, 93–103 (1964).
38. C. T. Prewitt, R. T. Down, High-pressure crystal chemistry. *Rev. Mineral.* **37**, 283–317 (1998).
39. T. A. Manz, N. G. Limas, Introducing DDEC6 atomic population analysis: Part 1. Charge partitioning theory and methodology. *RSC Adv.* **6**, 47771–47801 (2016).
40. B. Boates, S. A. Bonev, First-order liquid-liquid phase transition in compressed nitrogen. *Phys. Rev. Lett.* **102**, 015701 (2009).
41. D. Melicherová, O. Kohulák, D. Plašienka, R. Martoňák, Structural evolution of amorphous polymeric nitrogen from ab initio molecular dynamics simulations and evolutionary search. *Phys. Rev. Mater.* **2**, 103601 (2018).
42. C. Glass, A. Oganov, N. Hansen, USPEX—Evolutionary crystal structure prediction. *Comp. Phys. Comm.* **175**, 713–720 (2006).
43. G. Kresse, G. J. Hafner, *Ab initio* molecular dynamics for liquid metals. *Phys. Rev. B* **47**, 558–561 (1993).
44. G. Kresse, J. Furthmüller, Efficiency of ab-initio total energy calculations for metals and semiconductors using a plane-wave basis set. *Comput. Mater. Sci.* **6**, 15–50 (1996).
45. G. Kresse, J. Furthmüller, Efficient iterative schemes for ab initio total-energy calculations using a plane-wave basis set. *Phys. Rev. B* **54**, 11169–11186 (1996).
46. J. P. Perdew, K. Burke, M. Ernzerhof, Generalized gradient approximation made simple. *Phys. Rev. Lett.* **77**, 3865–3868 (1996).